

Temporally Smooth Mesh Extraction for Procedural Scenes with Long-Range Camera Trajectories using Spacetime Octrees

ZEYU MA, Princeton University, USA

ADAM FINKELSTEIN, Princeton University, USA

JIA DENG, Princeton University, USA

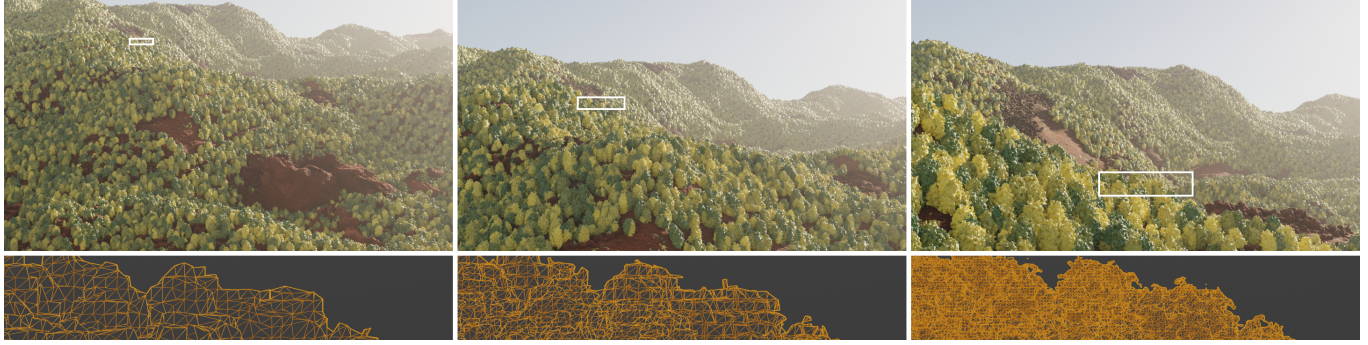


Fig. 1. We propose BinocMesher to extract temporally smooth 3D meshes from occupancy functions by slicing a 4D mesh. The first row shows sample images rendered from the meshes. The second row shows how the 3D mesh in the white boxed area gradually gains geometric detail as the camera moves closer to it.

The procedural occupancy function is a flexible and compact representation for creating 3D scenes. For rasterization and other tasks, it is often necessary to extract a mesh that represents the shape. Unbounded scenes with long-range camera trajectories, such as flying through a forest, pose a unique challenge for mesh extraction. A single static mesh representing all the geometric detail necessary for the full camera path can be prohibitively large. Therefore, independent meshes can be extracted for different camera views, but this approach may lead to popping artifacts during transitions. We propose a temporally coherent method for extracting meshes suitable for long-range camera trajectories in unbounded scenes represented by an occupancy function. The key idea is to perform 4D mesh extraction using a new spacetime tree structure called a binary-octree. Experiments show that, compared to existing baseline methods, our method offers superior visual consistency at a comparable cost. The code and the supplementary video for this paper are available at <https://github.com/princeton-vl/BinocMesher>.

CCS Concepts: • **Computing methodologies** → **Mesh models; Mesh geometry models; Antialiasing**.

Additional Key Words and Phrases: Procedural occupancy functions, mesh extraction, popping, 3D anti-aliasing, level-of-detail (LOD), smooth LOD transition, multiresolution representations, 4D octree, dual contouring

1 Introduction

Procedural approaches including occupancy functions are widely used in creating 3D content ranging from movies and games [Ebert et al. 2003; Perlin 2003; Smelik et al. 2014], to synthetic datasets for 3D vision [Greff et al. 2022; Raistrick et al. 2023; Wrenninge and Unger 2018]. Compared with alternatives such as scenes scanned from the real-world or modeled by artists, procedural approaches have the advantage of expressing complex and unbounded geometry with compact mathematical rules. One possible way to render procedural scenes represented by occupancy functions involves ray-marching. However, ray-marching into an unbounded occupancy

function requires small step sizes to avoid missing thin structures; and even so, adjacent pixels can produce inconsistent results. Therefore, it is often advantageous to extract and render triangle meshes. Moreover, meshes also offer compatibility with a broad range of rendering pipelines, ease of texturing, and familiarity for artists.

We address view-dependent mesh extraction for unbounded scenes with pre-defined long-range camera trajectories, such as flying through a vast forest or mountainscape (Fig. 1). Given a static occupancy function $f : \mathbb{R}^3 \mapsto \{0, 1\}$ and a camera trajectory at timestamps $\{t_i, i = 1, 2, \dots, L\}$, the goal is to extract a sequence of meshes $\{M_i\}$. To avoid popping artifacts, these meshes should be temporally smooth. We assume the camera path is known in advance, as in applications like animation and synthetic data generation.

A naive solution is to extract a single global mesh using methods such as OcMesher [Ma et al. 2025]. However, unbounded scenes with long-range camera trajectories can result in meshes so large as to exceed the capacity of extraction algorithms and rendering engines. To address this challenge, one could extract multiple meshes, one for each subsequence along the full trajectory, using OcMesher or other methods [Raistrick et al. 2023; Scholz et al. 2015]. However, severe popping can occur without an excessively high mesh resolution or a way to smoothly transition between the meshes. The *progressive meshes* approach of Hoppe [1996] affords a smooth transition called a *geomorph* between meshes of differing resolution. While this multi-resolution approach can reduce rendering cost, it begins by decimating the full-resolution mesh. Splitting a huge terrain into blocks and processing each block as a separate progressive mesh helps limit memory needed, but also creates challenges at block boundaries [Hoppe 1997].

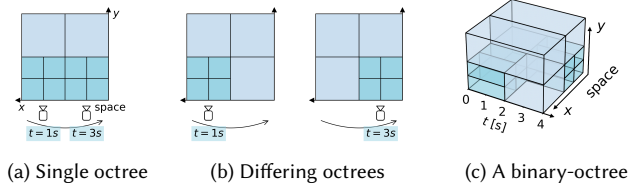


Fig. 2. Several options for a camera-dependent tree structures. The x and y spatial axes are labeled, while z is not shown. The binary-octree (c) supports the two spatial splits shown in (b) at different times.

This paper introduces **BinocMesher**, a spacetime tree-based mesh extraction algorithm. Instead of constructing a global octree [Meagher 1982] or multiple octrees in the 3D space, we partition the 4D spacetime into hypercubes, as shown in Fig. 2. By slicing this 4D structure in the time dimension, we can extract static meshes at different times. To avoid popping artifacts, it is crucial to perform this slicing task in a way that provides temporal coherence in the resulting meshes. Ponchio and Hormann [2008] observe (for uniform grids) that interpolation between two 3D meshes is equivalent to slicing a *4D mesh*, i.e., a polyhedral mesh embedded in 4D space-time. We extend this approach to multiresolution grids wherein we need to address the challenge of slicing neighboring regions of differing resolution. We introduce a new tree structure called **binary-octree**, where each non-leaf node either splits in the time dimension (into two children) or splits in the spatial dimensions (into eight children). In principle one could use a 4D hyper-octree which has 16 children at internal nodes [Puech and Yahia 1985], but this tree requires uniform spatial refinements at all times. Instead the binary-octree combines aspects of a K-D tree [Bentley 1975] and a 2^D tree, with each temporal split enabling different spatial splits in the two child nodes (Fig. 2c). This approach is more memory-efficient for long camera trajectories.

Our method proceeds in three steps, as illustrated in Fig. 3. First, we construct a binary-octree. Next, we extract a 4D mesh from the occupancy function evaluated at the spacetime-tree “corners” using dual contouring [Ju et al. 2002]. Finally, we slice the 4D mesh to generate 3D meshes at different timestamps. As the camera moves along its path, some polygons merge into a low-resolution shape, while other polygons split to provide more detail, as shown in Fig. 1. We control the visual consistency of the resulting 3D meshes by the size of the hypercube in the binary-octree. For example, if each hypercube spans at least two seconds in Fig. 3(a), then it must take at least two seconds to transform between meshes of adjacent levels of detail (LODs), e.g. meshes A-C in Fig. 3(c). We call this duration the *transition control parameter* δ_t , which balances between the goals of memory efficiency and temporal coherence.

Our contributions may be summarized as follows. We introduce a spacetime-octree-based mesh extraction algorithm to produce temporally smooth meshes for long-range camera trajectories. Second, we optimize the algorithm with efficient designs to minimize memory and computational costs. We also describe experiments showing that our method offers better visual consistency at a comparable cost to baseline methods.

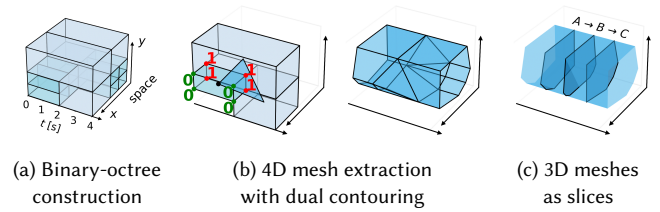


Fig. 3. Overview of BinocMesher

2 Related Work

Mesh Extraction. The *marching cubes* method of Lorensen and Cline [1998] extracts a mesh as an isosurface of an implicit function, and multiresolution methods support varying LOD for large scenes. One class of methods considers alternate grids using spherical coordinates [Raistrick et al. 2023], or constructing multiresolution grids of polyhedra [Gerstner and Pajarola 2000; Zhou et al. 1997] or tetrahedra [Pascucci and Cole-McLaughlin 2002; Weber et al. 2001]. Dual contouring offers an alternate approach that operates directly on arbitrary multiresolution grids, including spherical grids [Jang et al. 2022] and octree grids in arbitrary dimensions [Ju et al. 2002; Ju and Udeshi 2006; Ma et al. 2025; Perry and Frisken 2001; Wenger 2013]. Existing multiresolution mesh extraction methods – including the work of Jang et al. [2022], which shares a similar name with ours – focus on static meshes with fixed LODs. In contrast, BinocMesher offers temporally smooth mesh extraction from scenes with dynamic, camera-dependent LODs.

Geomorphs. Given a single mesh of the highest LOD, various approaches produce simplified meshes with smooth transitions, known as geomorphs. Early algorithms [Lindstrom et al. 1996; Taylor and Barrett 1994] address the specific case where the mesh is from a height field. Hoppe’s [1996] progressive mesh representation defines a continuous sequence of meshes of varying LOD, enabling efficient geomorphs between any pair. Subsequent efforts [El-Wajeh et al. 2022; Hoppe 1997; Sander and Mitchell 2006], including Nanite in Unreal Engine 5, extended these LOD control methods from a single monotonic scale to view-dependent LOD. Applying these methods to large scenes described by procedural occupancy functions requires an intractable intermediate mesh at the highest LOD.

3D Anti-aliasing. Beyond geomorphs, various 3D anti-aliasing techniques have been explored. Scholz et al. [2015] apply a spatially varying low-pass filter to modify the input function, which is limited to signed distance functions (and still admits aliasing). Giegl and Wimmer [2007] apply LOD blending in image space without accounting for 3D geometry. Infinigen [Raistrick et al. 2023] uses extremely high-resolution meshes in order to supersample the scene, which is an expensive approach in this context.

Spacetime Methods. Graphics research has a rich history that considers animated sequences in 4D spacetime for other purposes. For example, Glassner [1988] uses *spacetime raytracing* to render animation as a 4D scene. Cameron [1990] consider collision in 3D as a 4D intersection test. Schmid et al. [2010] propose a 4D structure to aggregate object motion for rendering motion blur and other effects. Du et al. [2021] recolor videos by slicing 4D polyhedral palettes.

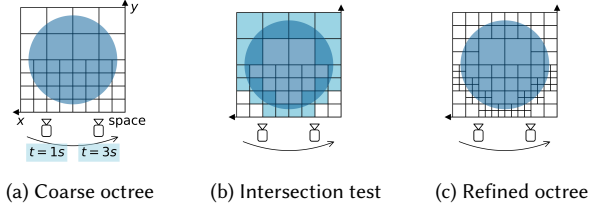


Fig. 4. OcMesher builds the octree from coarse to fine. Two of the spatial axes x and y are shown. (a) Cubes closer to the camera have larger projected diameter, and are therefore refined. (b) Nodes intersecting the surface are found. (c) Tree is refined around these intersections.

3 Preliminaries: Inputs, Octree and OcMesher

Our binary-octree construction process builds on the octree refinement approach of OcMesher [Ma et al. 2025], which generates a minimal number of polygons using a coarse-to-fine approach (Fig. 4). Therefore, we review the OcMesher framework before diving into the details of the binary-octree and its construction.

Inputs. OcMesher takes a pre-defined camera path and an occupancy function $f: \mathbb{R}^3 \mapsto \{0, 1\}$ as inputs. For example, the occupancy function for a sphere is $1[x^2 + y^2 + z^2 < r^2]$, where $1[\cdot]$ is the indicator function. With more complex techniques, a dense forest is modeled by collections of ellipsoids where the radii are perturbed by adding multi-octave Perlin noise $g(x, y, z)$ over the r^2 above.

Step a: Coarse Octree. OcMesher first constructs a coarse octree based on the projected angular diameter of each octree node \mathcal{N} as seen by the camera at each timestamp t_i . The angular diameter is approximated as $\mathcal{D}_N^{(i)}$, which is defined to be the ratio of the node size to the distance between the node and the camera:

$$\mathcal{D}_N^{(i)} = S_N / \|x_i - X_N\|, i = 1, 2, \dots, L \quad (1)$$

where x_i is the location of the camera at time t_i , X_N is the location of the cube center, and S_N is its side length.

A max-priority queue is initialized with a root node that is large enough to cover the whole scene. Throughout the splitting process, each queue entry corresponds to a single leaf node in the tree, prioritized by its maximum projected diameter over the entire trajectory:

$$\mathcal{D}_N = \max_{1 \leq i \leq L} \mathcal{D}_N^{(i)} \quad (2)$$

The algorithm iteratively extracts the top node, splits it into eight children, and re-inserts them into the queue until either the maximum diameter falls below a coarse threshold ($\mathcal{D}_N < \hat{D}_1$) or the

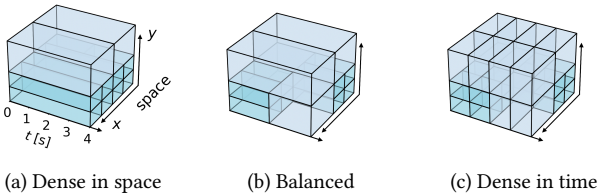


Fig. 5. Possible binary-octrees using different split decisions. A block of 3D spacetime is shown with two spatial axes x and y .

total number of nodes reaches a cap. The priority queue allows subdividing the largest nodes. Details appear in Sec. 6.1.

Step b: Intersection Test. OcMesher next identifies nodes intersecting the isosurface by evaluating the occupancy function at the corners of each node, seeking nodes that straddle “inside/outside”.

Step c: Refined Octree. OcMesher finally splits all nodes intersecting the surface, similar to Step (a), but with a smaller threshold.

4 Method: Binary-Octree and BinocMesher

This section provides an overview of how to extend the 3D approach of OcMesher to 4D, by splitting in the time dimension and thereby allowing for different spatial subdivisions at different times in a binary-octree. More details regarding efficient implementation are described in Section 6.

4.1 Binary-Octree

Internal binary-octree nodes split in one of two cases:

- **Spatial Splits:** The node contains eight children that uniformly partition the spatial range and span the same temporal range.
- **Temporal Splits:** The node contains two children that span the same spatial range but split the temporal range into halves.

Fig. 5 shows a block of 3D spacetime, with only two spatial axes. There are many possible binary-octrees, based on different splitting decisions. In Option (a) there are no temporal splits, which reduces to the octree solution and produces a dense spatial splitting. Option (c) shows dense temporal splits with too many tree nodes. Option (b) strikes balance between the 3D mesh size and the tree size. To achieve such a balance, we propose the following goals for deciding when to apply temporal splits:

- **Minimal Temporal Splits:** We apply temporal splits only when needed to allow for differing spatial splits in the two children.
- **Temporal Coherence:** A node should span at least a minimum duration set by the transition control parameter δ_t . We should avoid a temporal split that produces nodes of duration $< \delta_t$.

For a node \mathcal{N} with its time window $[T_N^0, T_N^1]$, instead of considering all the cameras, we compute its diameter only for cameras within its window. As illustrated in Fig. 6, we examine the list of $\mathcal{D}_N^{(i)}, T_N^0 \leq t_i \leq T_N^1$. If there is a subsequence that consists of diameters smaller than a threshold (half of the maximum diameter), and it

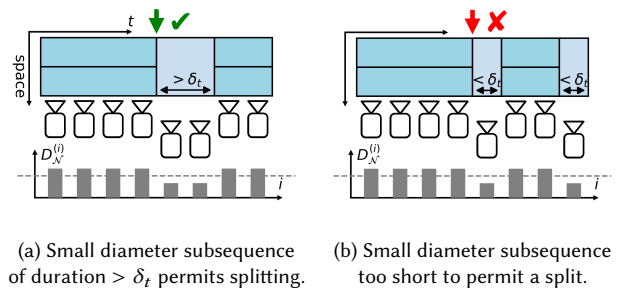


Fig. 6. Proposed temporal coherence criterion.

ALGORITHM 1: Alternating Temporal and Spatial Splits

Input: Root spacetime node \mathcal{N}_0 ; Diameter threshold \hat{D} .
Output: Binary-octree with nodes satisfying threshold \hat{D} .

```

1  $Q \leftarrow \{\}$  // create an empty max-priority queue
2  $\mathcal{N} \leftarrow \mathcal{N}_0$ 
3 while  $\mathcal{D}_{\mathcal{N}} > \hat{D}$  do
4   if temporal_split_test( $\mathcal{N}$ ) // see Fig. 6
5     then
6        $\{\mathcal{N}_1, \mathcal{N}_2\} \leftarrow \text{temporal\_split}(\mathcal{N})$ 
7       for  $i = 1, 2$  do
8         enqueue( $Q, \mathcal{N}_i$ )
9     else
10       $\{\mathcal{N}_1, \mathcal{N}_2, \dots, \mathcal{N}_8\} \leftarrow \text{spatial\_split}(\mathcal{N})$ 
11      for  $i = 1, 2, \dots, 8$  do
12        enqueue( $Q, \mathcal{N}_i$ )
13       $\mathcal{N} \leftarrow \text{dequeue}(Q)$ 
14 return  $\mathcal{N}_0$ 

```

spans at least duration δ_t , we may separate this sequence via temporal splits (Fig. 6a). This would avoid equivalent spatial splitting over the whole sequence, saving overall memory. Otherwise, if either diameters are similar across the sequence or the subsequences are too short (Fig. 6b), temporal splits are not applied.

A max-priority queue is used to construct the binary-octree, prioritized by $\mathcal{D}_{\mathcal{N}}$, generalizing OcMesher and equation (2) to consider only a subsequence of camera frames. Temporal and spatial splits are performed alternately, with temporal split tests preceding spatial splits for newly split nodes, as described in Algorithm 1.

4.2 Coarse-to-fine Algorithm

Similar to OcMesher, a coarse-to-fine algorithm is used to construct a refined binary-octree.

Step a: Coarse Binary-Octree. First, we apply Algorithm 1 to a root spacetime node with a coarse diameter threshold \hat{D}_1 . The root node encompasses a large spatial extent and all camera timestamps.

Step b: Intersection Test. Next, we identify nodes intersecting the isosurface by evaluating the occupancy function at the 16 corners of the hypercube represented by each node. Checking every node is expensive, so following OcMesher, we accelerate this step using flood-fill approach. We select a subset of the nodes as seeds and iteratively propagate from any surface-intersecting node to both spatial and temporal neighbors. Spatial flooding ensures no spatial discontinuities occur, while temporal flooding prevents temporal inconsistencies that would lead to popping effects.

Step c: Refined Binary-Octree. Finally, we refine the binary-octree by reapplying Algorithm 1 independently to each surface-intersecting node, now using a smaller threshold $\hat{D}_2 < \hat{D}_1$.

4.3 4D Mesh Extraction

Dual Contouring. In K -dimensional dual contouring, each *surface-intersecting* hypercube (having different corner values) corresponds to a mesh vertex. Each *bipolar edge* (connecting different values) is associated with a $(K - 1)$ -dimensional polyhedron (polytope) embedded in K -dimensional space. In the 3D case illustrated in

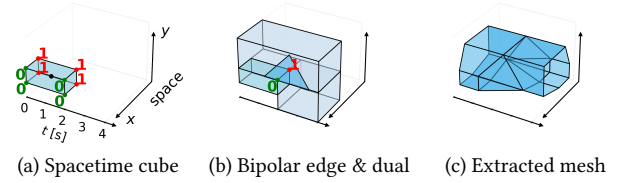


Fig. 7. Block of 3D spacetime with the two spatial axes x and y . (a) Dual contouring associates each surface-intersecting node with a vertex, and (b) each bipolar edge with a dual polygon. Extracted mesh shown in (c).

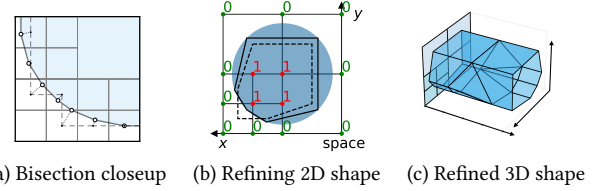


Fig. 8. Placing vertices at hypercube centers leads to “staircase” artifacts (dashed lines). We use bisection to project these vertices closer (solid lines) to the true geometry. (a) A close-up 2D example, where the cube centers (filled dots, dashed lines) after bisection move close to the true shape (hollow dots, solid lines). (b) Extracting the full 2D shape – a blue circle, on a coarser grid than in (a). (c) The 3D shape from Fig. 7c refined after bisection search.

Fig. 7, each bipolar edge is associated with a polygon and a 3D mesh consists of many polygons. In the 4D case for the binary-octree, each bipolar edge is associated with a polyhedron embedded in 4D space. Such a polyhedron can be a hexahedron with 8 vertices in general, or other forms with fewer vertices. A 4D mesh consists of many polyhedra.

Vertex Computation by Bisection: We extract one vertex per hypercube. Placing it at the center would lead to “staircase” artifacts illustrated by the dashed lines in Fig. 8(a-b). For discrete scalar data, interpolation-based methods [Lorenson and Cline 1998] are suitable for placing mesh vertices; however, they are not effective for a point-wise binary occupancy function over \mathbb{R}^3 . Instead, we use bisection. For a binary function in 1D, bisection reduces to binary search to pinpoint a 0-1 transition. Similarly, we use bisection in 3D to project the vertex close to the actual surface (shown as solid lines).

4.4 Mesh Slicing

Figures 9 and 10 illustrate by analogy mesh slicing in 3D and 4D. Fig. 9 shows at a given timestamp finding polygons intersecting the slicing plane, producing line segments at the intersections. This set of line segments forms a 2D “mesh” (set of polygons). Fig. 10 shows how in 4D spacetime we find polyhedra intersecting the slicing plane. A polyhedron can be a hexahedron embedded in 4D with eight vertices (or other forms with fewer vertices) and its vertices can follow a complex temporal ordering (Fig. 10). To slice such a polyhedron with a plane at $t = t_1$, we find edges (u, v) where $t_u \leq t_1 < t_v$ and place an intersection vertex for each edge. Each face of the polyhedron has 0, 2, or 4 intersection vertices and we connect them to form one or more polygons. These polygons form

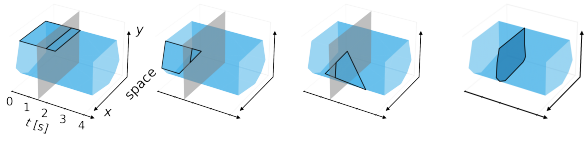


Fig. 9. In 3D spacetime, we extract line segments by slicing polygons, and the output segments form a set of polygons.

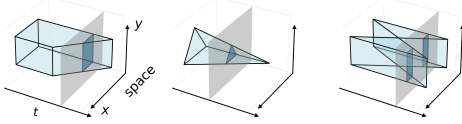


Fig. 10. In 4D spacetime (drawn here in 3D), we extract polygons by slicing polyhedra, and the output polygons form a mesh. Shown are several different polyhedron types, resulting in different shapes and numbers of polygons.

a mesh in 3D. This mesh gradually transforms as the slicing plane moves through time.

5 Experiments

The supplementary video shows several scenes as animations.

Input Scenes. We use the procedural terrain from Infinigen [Raistrick et al. 2023], along with additional modeling techniques [Quilez 2022] [otaviogood 2015], to create camera animations of complex scenes, including *Forest*, *Mountain*, *Arctic*, *Cave*, *Beach*, and *City*.

Parameters. Each video spans 20 seconds at 24 frames per second and a resolution of 960×540. We set the transition control parameter $\delta_t = 1$ s and the diameter threshold $\hat{D}_2 = 3$ px. The user can adjust these parameters according to their needs. Additional efficiency-related parameters in Sec. 6 are available but set to defaults.

Baselines. We compare BinocMesher against two baselines:

- **Spherical:** Spherical Mesher is used by default in Infinigen and constructs uniform grids in spherical coordinates and applies the marching cubes algorithm. A mesh is extracted every 8 frames.
- **OcMesher:** OcMesher divides the camera trajectory into subsequences, and extracts a single mesh for each subsequence. We experiment with subsequence lengths of 24 and 96 frames, referred to as **OcMesher-24** and **OcMesher-96**, respectively.

5.1 Visual Consistency

Fig. 11 shows frames of the *Forest* scene comparing the four methods. Zoomed-in squares show the region boxed in white, comparing it with the same region in the next frame of the animation. Each frame is selected as the *second worst* from the whole animation for each method, according to a visual consistency score. This score is visualized in the heatmap on the right (bright is worse) and computed as follows. The score of frame i , denoted S_i , measures the consistency between frame i and the next frame $i + 1$:

$$S_i = \text{SSIM}(I_i, \text{warp}(I_{i+1}, F_{i \rightarrow i+1})) \quad (3)$$

where $F_{i \rightarrow i+1}$ is the ground-truth optical flow, I_i and I_{i+1} are consecutive rendered images, function **warp** warps a given image via the

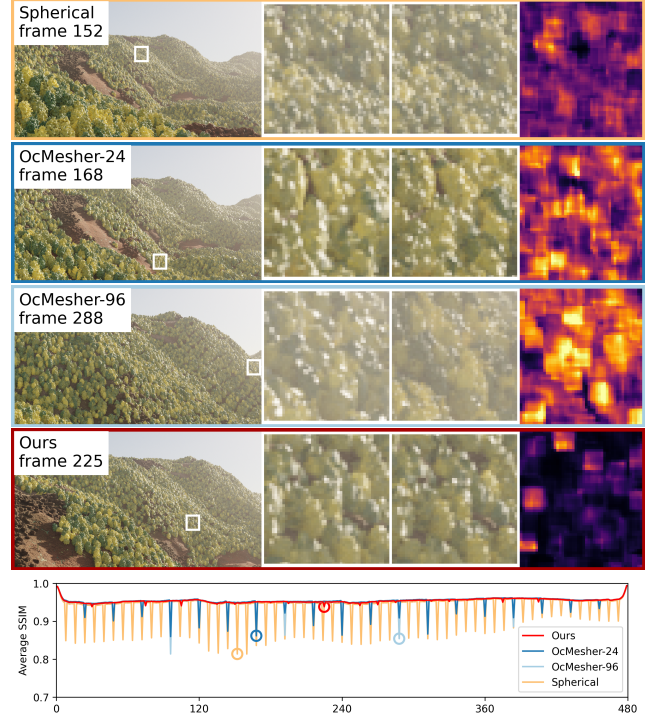


Fig. 11. *Above:* For each method (color coded), the second worst frame according to SSIM view consistency scores. The zoomed-in squares compare this frame to the subsequent one, followed by their SSIM heatmap (brighter is worse). These squares highlight the worst (SSIM) region in each frame. *Below:* Average SSIM for each frame, graphed across the entire sequence, for the four methods. Lower is worse. Valleys indicate popping. Circles note the SSIM at the four frames selected above.

inverse map of the forward flow (to avoid resulting gaps), and **SSIM** is the Structural Similarity Index Measure [Wang et al. 2004].

The plot in Fig. 11 shows the average score S_i for each frame, with circles identifying S_i for the four frames above, color coded by method. Spherical, OcMesher-24 and OcMesher-96 update the mesh for each subsequence of frames, resulting in the periodic “valleys” in both plots that signify “popping” events. While a larger subsequence length in OcMesher-96 reduces the frequency of popping relative to OcMesher-24, it increases the severity of each occurrence. In contrast, our method maintains consistently high S_i and small normal difference, with only minor valleys (and in other scenes, our method exhibits even fewer valleys). Each valley’s severity is evaluated by $S_{i-1} + S_{i+1} - 2S_i$, and this is the measure by which these circled valleys are the second worst for each method in the sequence. The worst frames for each sequence are shown for all four methods in all six scenes in Figures 18 and 19. Alternatively, Figures 20 shows a direct comparison at the same frame.

Fig. 12 illustrates geometric consistency of the four methods using geometry-only (*clay-style*) renderings, with corresponding normal difference heatmaps (where brighter is worse). The plot shows average surface normal differences (in degrees). The normal difference

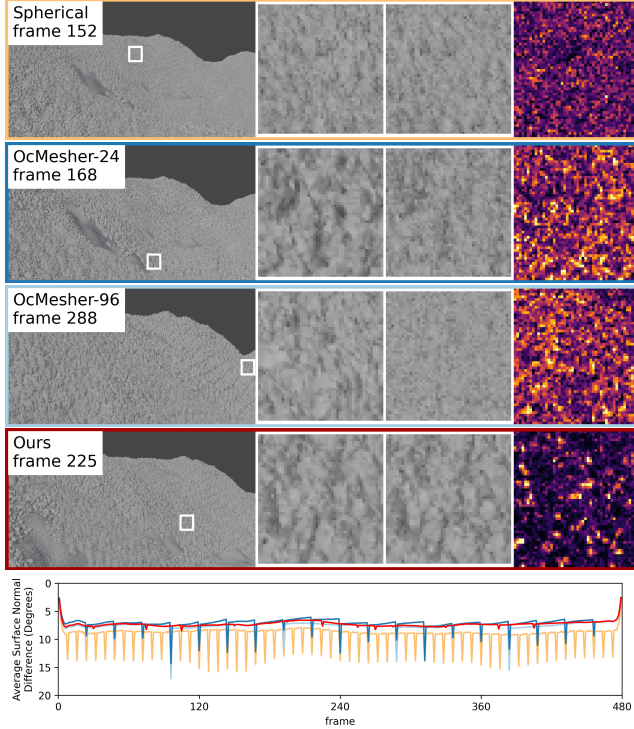


Fig. 12. *Above*: For each method, geometry-only (*clay-style*) rendering of the frames in Fig. 11, followed by their normal difference heatmap (brighter is worse). *Below*: Plot of average normal difference, which is highly correlated with the SSIM plot shown in Fig. 11.

is highly correlated with **SSIM** (Fig. 11), and slightly noisier, so we only report the latter throughout the rest of the paper.

5.2 Computational Cost

This section presents experiments comparing the performance of the four methods; Sec. 6.3 describes the theoretical complexity of our algorithm. All methods run on a multi-core CPU, with occupancy queries performed on the GPU. Table 1 compares the runtime and the vertex count of the four methods for the *Forest* scene. The runtime is divided into two parts: mesh generation (meshing) and rendering. Meshing cost is reported as amortized per frame. While rendering is not part of these mesh extraction methods, it remains the bottleneck.

Spherical Mesher has the longest overall runtime due to a high mesh resolution that mitigates popping, but it still has much more popping than the other methods. OcMesher generate meshes faster than our method. However, as the subsequence length increases, though OcMesher-96 does less work for the entire sequence than OcMesher-24, it creates a larger mesh for each frame. This increases the risk of exceeding the memory limits and results in longer rendering time than ours. Overall, our method has a comparable cost, while offering better view consistency.

The components of meshing time for our method are roughly: 3% for constructing the binary-octree, 32% for extracting the 4D mesh,

Table 1. Computational cost of the four methods. Measured on 64-core 12th Gen Intel Core i7 CPU with RTX 2080. Our method offers better view consistency (Fig. 11) with comparable overall cost.

	Spherical	OcMesher-24	OcMesher-96	Ours
Runtime (sec/frame)				
Meshing (Amortized)	21	7	3	23
Rendering	254	193	220	199
Total	275	200	223	222
Vertex Count				
Total from all Blocks	565 M	105 M	55 M	81 M
Average Per Frame	9.1 M	5.2 M	10.9 M	9.3 M

Table 2. Larger values of t_0 have similar total runtime, but produce larger meshes, which increases the risk of exceeding the memory limits.

Parameter δ_t	0.5	1.0	2.0	4.0
Runtime (sec/frame)				
Meshing (Amortized)	27	23	22	16
Rendering	195	199	200	205
Total	222	222	222	221
Vertex Count				
Total	103 M	81 M	66 M	54 M
Averaged Per Frame	7.0 M	9.3 M	13.8M	20.5M

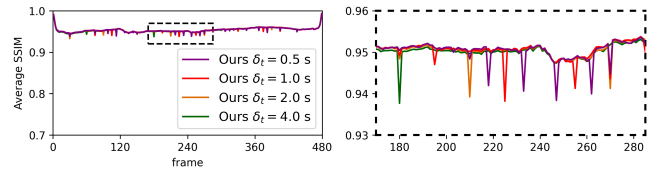


Fig. 13. Effect of δ_t on S_i . Larger δ_t has less frequent valleys (but all δ_t have relatively small valleys). Dashed box enlarged on right.

and the remaining 65% for slicing the mesh. Greater GPU utilization is possible but not a current bottleneck.

5.3 Transition Control Parameter Settings

The transition control parameter δ_t balances between the goals of memory efficiency and temporal coherence. Here we evaluate this tradeoff for different values of δ_t . In Fig. 13, the SSIM score plots for larger δ_t have less frequent valleys. In Table 2, larger δ_t values produce larger 3D meshes per frame, leading to increased risk of exceeding the memory limits. Considering these factors, $\delta_t = 1s$ remains a balanced choice with relatively infrequent and small consistency score fluctuations as well as lower memory usage. Therefore we use this value in our other experiments. However, users with a larger memory budget can opt for a larger δ_t .

6 Implementation Details

This section describes some strategies for efficient implementation of the Binary-Octree algorithms introduced in Section 4.

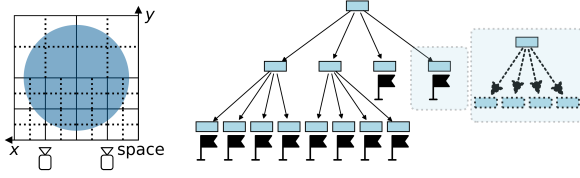


Fig. 14. When the coarse tree reaches a certain size cap, nodes are flagged as *virtual grids* to save computation. Only two spatial axes are shown.

6.1 Efficient Implementation of Tree Construction

One goal of the coarse-to-fine binary-octree construction algorithm is to prioritize allocating resources to regions of the scene relevant to rendering. To this end we employ several implementation strategies.

Virtual Grid. Given a fixed diameter threshold \hat{D}_2 , the intermediate (coarse) threshold \hat{D}_1 plays a crucial role in the coarse-to-fine tree construction algorithm. A large \hat{D}_1 reduces the coarse tree’s memory usage; while a smaller value produces finer surface-intersecting nodes, reducing subsequent refining costs. To balance these trade-offs, we adopt the virtual grid technique from OcMesher.

In 4D spacetime, when a coarse binary-octree reaches a certain size cap C , we halt refinement and simply flag any node \mathcal{N} that requires further splits (i.e., $\mathcal{D}_{\mathcal{N}} > \hat{D}_1$), as illustrated in Fig. 14. The flag marks the node as a “virtual” grid of size $V^3 \times 1$, where V is the smallest power of 2 such that $\mathcal{D}_{\mathcal{N}} < V\hat{D}_1$. By combining the virtual grid with the flood-fill algorithm, surface intersection tests are performed at fine granularity without the memory overhead of actually refining the tree everywhere. During refinement, only surface-intersecting virtual nodes are instantiated. Our experiments use $\hat{D}_1 = 30$ px and size cap $C = 10M$.

Contraction Out of Frustum. To avoid unneeded detail outside the camera frustums, we contract the computed camera-specific node diameter $\mathcal{D}_{\mathcal{N}}^{(i)}$ of any node outside the frustum by a small factor throughout tree construction. Our experiments use factor $\frac{1}{4}$.

Visibility Test with Depth Buffers. To further avoid unnecessary detail, we optionally use a depth buffer for each camera during the surface-intersection test. We omit portions of the surface that are known to be occluded in all camera views. For each surface-intersecting node, we project a proxy onto each depth buffer (in the node’s time window) to identify visible nodes for subsequent refinement. While this optimization fails for scenes with transparency or intricate structure near silhouettes, we find it effective in many scenarios and include it in our experiments.

6.2 Node Groups and Dual Polyhedron Search

For long-range camera sequences, the refined binary-octree contains too many nodes to fit into RAM. Therefore, we organize the coarse nodes into groups based on their **temporal range**. In the subsequent steps, bipolar edge search and polyhedron extraction, coarse nodes are loaded group by group with their refined child nodes.

We name the groups with *binary encoding*, as shown in Fig. 15. The group \mathcal{G} represented by the root node spans the entire time range. The left and right children of \mathcal{G} , each spanning half that

Root											
0						1					
00		01		10		11		00		01	
000	001	010	011	100	101	110	111	0000	0001	0010	0011
								0100	0101	0110	0111
								1000	1001	1010	1011
								1100	1101	1110	1111

Fig. 15. We group coarse nodes / hypercubes with binary encodings of its temporal range. For a bipolar edge in group “10” (in pink), it may have neighboring hypercubes in colored groups as formulated in Eq. 4.

range, are \mathcal{G}_0 and \mathcal{G}_1 . In general, the left child of \mathcal{G}_s is \mathcal{G}_{s0} , and the right child is \mathcal{G}_{s1} – by appending either 0 or 1 to string s .

The dual polyhedron of a bipolar edge has its vertices in the neighboring hypercubes of the edge (Fig. 7b). First, we note which groups neighbor the edge, then we propose efficient algorithms to find bipolar edges and extract dual polyhedra.

Neighboring Relation of Groups. Given a bipolar edge located in a coarse node in \mathcal{G}_s (the edge may lie on some refined hypercube edges, either on time boundary or in the middle). Consider, e.g., $s = “10”$ – the pink cube in Fig. 15. Its neighboring cubes can be in its children (yellow), or ancestors (gray), or on the left (blue), or on the right (green), or ancestors of the left and right (gray). Denoting the set of groups neighboring \mathcal{G}_s as \mathfrak{N}_s , we have:

$$\begin{aligned} \mathfrak{N}_s = & \{ \mathcal{G}_s \} \cup \text{descendants}(\mathcal{G}_s) \cup \text{ancestors}(\mathcal{G}_s) \\ & \cup \{ \mathcal{G}_{s-1} \} \cup \text{right_branch}(\mathcal{G}_{s-1}) \cup \text{ancestors}(\mathcal{G}_{s-1}) \\ & \cup \{ \mathcal{G}_{s+1} \} \cup \text{left_branch}(\mathcal{G}_{s+1}) \cup \text{ancestors}(\mathcal{G}_{s+1}) \end{aligned} \quad (4)$$

where **right_branch**(\mathcal{G}_s) are children of \mathcal{G}_s labeled by appending a sequence of 1’s to s ; and **left_branch**(\mathcal{G}_s) by appending 0’s. We use the notation $s - 1$ and $s + 1$ to mean: convert the encoding to integers, subtract or add one, then convert back to the binary string of the same length (possibly with leading 0’s).

Dual Polyhedron Search. We visit all groups in lexicographic order, and find bipolar edges by checking each hypercube edge in the group if it connects different values (+/−). When we find a new edge while visiting group \mathcal{G}_s , we visit the set \mathfrak{N}_s to find its neighboring hypercube. Because of the lexicographic traversal, we only need to visit the subset

$$\tilde{\mathfrak{N}}_s = \{ \mathcal{G}_r \in \mathfrak{N}_s | r \leq s \} \quad (5)$$

because larger ones are visited later. This omits the descendants and the third row in equation (4) – the yellow, the green, and potentially some gray groups. This process is summarized in Algorithm 2.

Bipolar Edge propagation. Fig. 16-left shows a 3D spacetime scenario where a bipolar edge lying on an edge of the narrow cubes

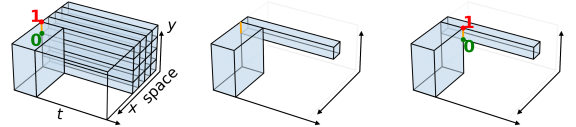


Fig. 16. *Left:* A type 1 bipolar edge lie on one of the cube edges; *Middle:* The neighboring nodes of this type 1 edge; *Right:* we offset the type 1 edge based on its neighbors to get a type 2 bipolar edge.

ALGORITHM 2: Dual Polyhedron Search

Input: A binary-octree with temporal tree depth d .
Output: The set of bipolar edges with dual polyhedra.

```

1 bipolar_edges  $\leftarrow$  {}
2 all_strings  $\leftarrow$  lex-ordered list of all binary strings of length  $\leq d$ 
3 for  $s$  in all_strings do
4   load_group( $\mathcal{G}_s$ )
5   new_edges  $\leftarrow$  bipolar edges at cube edges of  $\mathcal{G}_s$ 
6   bipolar_edges  $\leftarrow$  bipolar_edges  $\cup$  new_edges
7   Compute  $\tilde{\mathfrak{N}}_s$  as in Eq. (4) (5)
8   for  $\mathcal{G}_r \in \tilde{\mathfrak{N}}_s$  do
9     load_group( $\mathcal{G}_r$ )
10    for  $e \in$  bipolar_edges do
11      Find neighboring nodes of  $e$  within  $\mathcal{G}_r$ 
12      Bipolar edge propagation // see text
13 return bipolar_edges

```

(referred to as *type 1*) will be found in line 5. However, this may overlook bipolar edges of other types: Fig. 16-right shows another bipolar edge not on any cube edge (referred to as *type 2*). To find bipolar edges of type 2, we need to propagate from an existing type 1 edge e (line 12 in Algorithm 2). After we found the neighboring hypercubes of e , we offset the time coordinate by the smallest window size of its neighbors and add a new bipolar edge.

6.3 Memory and Time Complexity

Similar to OcMesher, the memory footprint of the BinocMesher depends on the complexity of the scene and how fast the camera rotates. Faster camera movement increases temporal division in the tree. However, memory requirements are insensitive to the length of the sequence, because Algorithm 2 only loads into memory the needed binary-octree node groups (not the entire binary-octree).

In terms of time complexity, the outer loop in Algorithm 2 considers all binary strings, which is $O(2^d)$ for *temporal tree depth* d (considering only temporal splits in the coarse binary-octree). The inner loop loads neighbors $\tilde{\mathfrak{N}}_s$, of which there are $O(d)$. Thus, the algorithm performs loading operations a total of $O(d \cdot 2^d)$ times. Moreover, in practice we find it maintains a bounded set of unresolved bipolar edges, making lines 6 and 10 take constant time. Depth $d = O(\log T)$, where T is the camera sequence duration. Therefore, the algorithm has overall time complexity $O(T \log T)$ with respect to duration, and thus scales gracefully to long sequences.

7 Discussion, Limitations and Future Work

BinocMesher addresses the temporal coherence challenge for mesh extraction in procedural scenes with long camera paths by slicing a 4D mesh. It offers better view consistency than baselines at similar cost. The proposed approach has a number of limitations, some of which suggest areas for future work.

Inputs. Our method is limited to predefined camera trajectories and fuzzy regions around them (discussed later), thereby excluding interactive applications like games. Nonetheless, offline rendering applications are prevalent in practice, including animation, video production, and synthetic data generation.

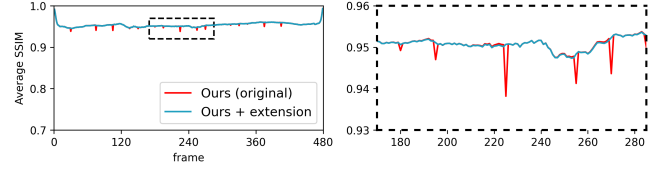


Fig. 17. An extension to our algorithm ameliorates minor popping artifacts in our method (small valleys in plot). Dashed box enlarged on right.

Dynamic Scenes. We can add dynamic effects into the static scene through animated displacement maps, like the ocean waves in the *Beach* scene. Moreover, since we ultimately render from a polygon mesh, it is also easy to add any animated characters or scene elements independent of the binary-octree like the crabs in the *Beach* scene. (See the supplementary video.) However, if the occupancy function itself is dynamic, applying LOD transition algorithms via BinocMesher reduces to one octree per frame.

Ray-Marching. We extract a polygon mesh for rendering. In principle, it might be possible ray-march directly into the procedural occupancy function, and thereby obviate the need for mesh extraction. But ray marching algorithms are typically constrained to a finite volume [Aaltonen 2018; Crassin et al. 2009; Gobbetti et al. 2008; Wald et al. 2016] or dependent on distance values [Galin et al. 2020; Hart 1996; Musgrave 2003; Seyb et al. 2019; Söderlund et al. 2022], and adjacent pixels can produce inconsistent results. Nevertheless, one could imagine a hybrid approach that might use ray marching, but leveraging a spatio-temporal tree akin to the Binary-Octree, to allow for varying step sizes.

Extension to Fuzzy Camera Paths. Our algorithm naturally extends to fuzzy camera paths because it takes a list of keyframe cameras with timestamps as input. Thus, instead of one camera for each keyframe, we could sample cameras covering the fuzzy region for each keyframe. Then the algorithm itself would remain unchanged, with runtime depending on the size of the fuzzy region rather than the number of sampled cameras due to GPU parallelization. In this way, a suitably high-resolution mesh could be provided so long as the actual camera path stays near the fuzzy path. Rendering from a camera path outside this region would result in graceful degradation in quality as the camera moves further away.

Extension to Ameliorate Popping Artifacts. The minor popping artifacts of our method revealed as small valleys in the SSIM plots are caused by new polygonal structures emerging discontinuously as zero-volume, double-sided slices. These structures come from faces in the polyhedra that are perpendicular to the time axis. To ameliorate such popping, we extend the algorithm to extrude these time-orthogonal faces into pyramidal volumes. Fig. 17 shows the effectiveness of this extension in the *Forest* scene.

Acknowledgments

This work was partially supported by the National Science Foundation under Award 2450506. Icons from Noun Project (CC BY 3.0): “Video Camera” by JS; “Flag” by Mike Zuidgeest.

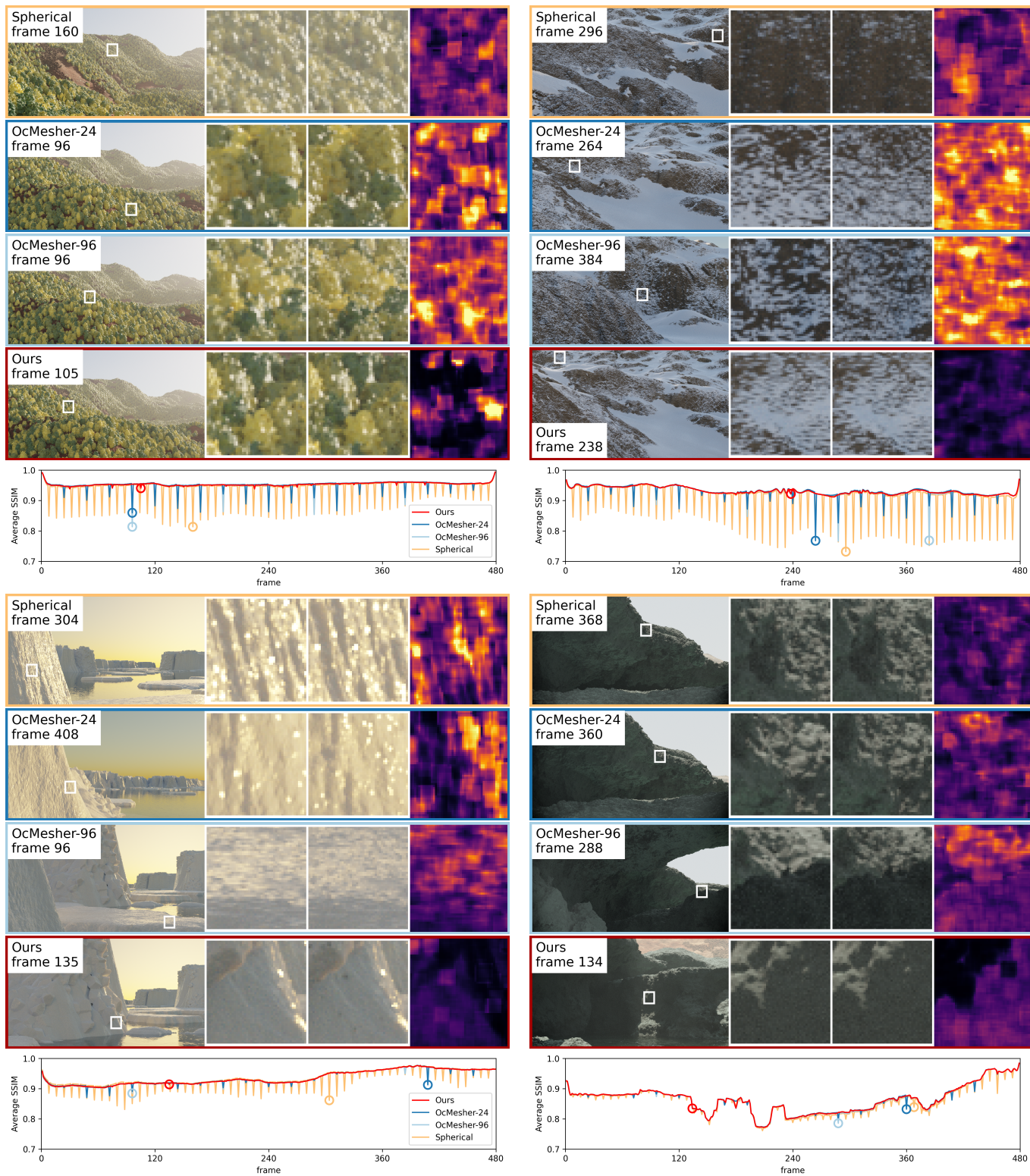


Fig. 18. The *worst* frames by SSIM for each method in the *Forest*, *Mountain*, *Arctic*, and *Cave* scenes. See Section 5.1 and Fig. 11 for explanation of figure components. Note that insufficient sampling in dark regions produces considerable visual noise in the *Cave* scene, which contributes to degraded SSIM scores for all methods in parts of this scene. While the advantage of our method is not as pronounced for *Cave* as for other scenes, it remains apparent in the plot.

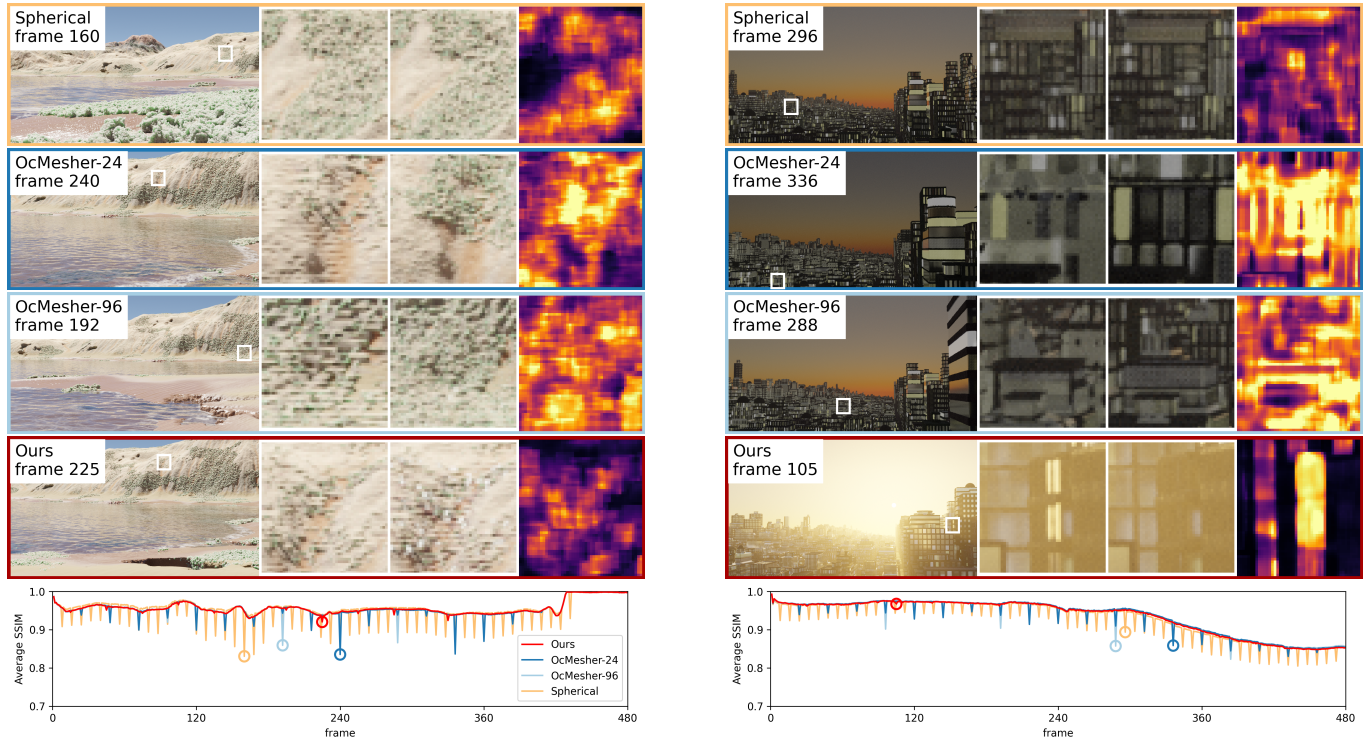


Fig. 19. The *worst* frames by SSIM for each method in the *Beach* and *City* scenes. See Section 5.1 and Fig. 11 for explanation of figure components. Note that the ocean waves are added as animated displacement and texture over the static water surface (see the supplementary video for the animated scene). Urban scenes are also modeled using occupancy functions. In these two challenging scenes, while the advantage of our method is not pronounced in the zoomed-in window, it remains apparent in the plot.

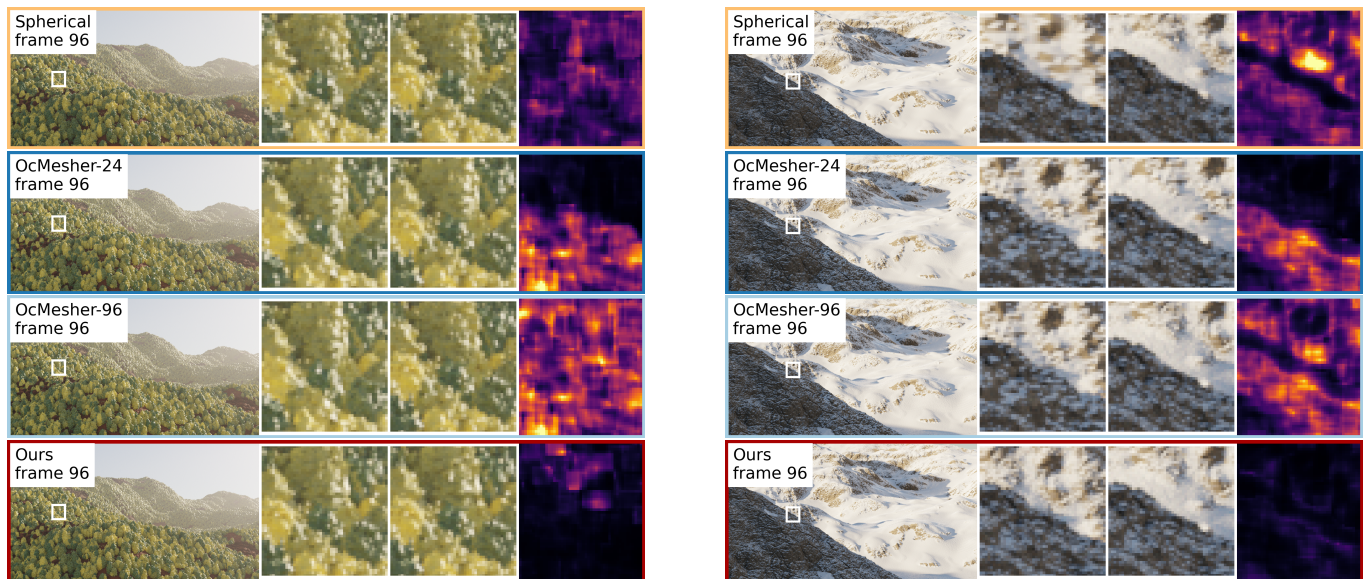


Fig. 20. For a more direct comparison, we align the time splitting (temporal discontinuities) in our method with the others, and compare the same zoomed-in window at a specific frame in the *Forest* and *Mountain* scenes. This may not be “fair” because the choice of frame or zoom can always favor one method. This is the 96th frame, when all four methods suffer from temporal discontinuities, and the zoom is chosen to show differences between the OcMesher versions.

References

- Sebastian Aaltonen. 2018. GPU-based clay simulation and ray-tracing tech in Claybook. *San Francisco, CA* 2, 5 (2018).
- Jon Louis Bentley. 1975. Multidimensional binary search trees used for associative searching. *Commun. ACM* 18, 9 (1975), 509–517.
- Stephen Cameron et al. 1990. Collision detection by four-dimensional intersection testing. (1990).
- Cyril Crassin, Fabrice Neyret, Sylvain Lefebvre, and Elmar Eisemann. 2009. Gigavoxels: Ray-guided streaming for efficient and detailed voxel rendering. In *Proceedings of the 2009 symposium on Interactive 3D graphics and games*. 15–22.
- Zheng-Jun Du, Kai-Xiang Lei, Kun Xu, Jianchao Tan, and Yotam I Gingold. 2021. Video recoloring via spatial-temporal geometric palettes. *ACM Trans. Graph.* 40, 4 (2021), 150–1.
- David S Ebert, F Kenton Musgrave, Darwyn Peachey, Ken Perlin, and Steve Worley. 2003. *Texturing & modeling: a procedural approach*. Morgan Kaufmann.
- Yasin AM El-Wajeh, Paul V Hatton, and Nicholas J Lee. 2022. Unreal Engine 5 and immersive surgical training: translating advances in gaming technology into extended-reality surgical simulation training programmes. *British Journal of Surgery* 109, 5 (2022), 470–471.
- Eric Galin, Eric Guérin, Axel Paris, and Adrien Peytavie. 2020. Segment tracing using local Lipschitz bounds. In *Computer Graphics Forum*, Vol. 39. Wiley Online Library, 545–554.
- Thomas Gerstner and Renato Pajarola. 2000. *Topology preserving and controlled topology simplifying multiresolution isosurface extraction*. IEEE.
- Markus Giegl and Michael Wimmer. 2007. Unpopping: Solving the image-space blend problem for smooth discrete LOD transitions. In *Computer Graphics Forum*, Vol. 26. Wiley Online Library, 46–49.
- Andrew S Glassner. 1988. Spacetime ray tracing for animation. *IEEE Computer Graphics and Applications* 8, 2 (1988), 60–70.
- Enrico Gobbetti, Fabio Marton, and José Antonio Iglesias Guitián. 2008. A single-pass GPU ray casting framework for interactive out-of-core rendering of massive volumetric datasets. *The Visual Computer* 24 (2008), 797–806.
- Klaus Greff, Francois Belletti, Lucas Beyer, Carl Doersch, Yilun Du, Daniel Duckworth, David J Fleet, Dan Gnanapragasam, Florian Golemo, Charles Herrmann, et al. 2022. Kubric: A scalable dataset generator. In *Proceedings of the IEEE/CVF Conference on Computer Vision and Pattern Recognition*. 3749–3761.
- John C Hart. 1996. Sphere tracing: A geometric method for the antialiased ray tracing of implicit surfaces. *The Visual Computer* 12, 10 (1996), 527–545.
- Hugues Hoppe. 1996. Progressive meshes. In *Proceedings of the 23rd Annual Conference on Computer Graphics and Interactive Techniques (SIGGRAPH '96)*. Association for Computing Machinery, New York, NY, USA, 99–108. doi:10.1145/237170.237216
- Hugues Hoppe. 1997. View-dependent refinement of progressive meshes. In *Proceedings of the 24th annual conference on Computer graphics and interactive techniques*. 189–198.
- Hyeonjoong Jang, Andreas Meuleman, Dahyun Kang, Donggun Kim, Christian Richardt, and Min H Kim. 2022. Egocentric scene reconstruction from an omnidirectional video. *ACM Transactions on Graphics (TOG)* 41, 4 (2022), 1–12.
- Tao Ju, Frank Losasso, Scott Schaefer, and Joe Warren. 2002. Dual contouring of hermite data. In *Proceedings of the 29th annual conference on Computer graphics and interactive techniques*. 339–346.
- Tao Ju and Tushar Udesi. 2006. Intersection-free contouring on an octree grid. In *Proceedings of Pacific graphics*, Vol. 2006. Citeseer.
- Peter Lindstrom, David Koller, William Ribarsky, Larry F Hodges, Nick Faust, and Gregory A Turner. 1996. Real-time, continuous level of detail rendering of height fields. In *Proceedings of the 23rd annual conference on Computer graphics and interactive techniques*. 109–118.
- William E Lorensen and Harvey E Cline. 1998. Marching cubes: A high resolution 3D surface construction algorithm. In *Seminal graphics: pioneering efforts that shaped the field*. 347–353.
- Zeyu Ma, Alexander Raistrick, Lahav Lipson, and Jia Deng. 2025. Mesh Extraction for Unbounded Scenes Using Camera-Aware Octrees. In *2025 International Conference on 3D Vision (3DV)*. IEEE, 845–854.
- Donald Meagher. 1982. Geometric modeling using octree encoding. *Computer graphics and image processing* 19, 2 (1982), 129–147.
- F Kenton Musgrave. 2003. QAEB Rendering for Procedural Models. In *Texturing & Modeling: A Procedural Approach*, David S. Ebert, Kurt Musgrave, Darwyn Peachey, Ken Perlin, and Ken Worley (Eds.). Morgan Kaufmann, 509–528.
- otaviogood. 2015. *Skyline*. Shadertoy. <https://www.shadertoy.com/view/XtsSWS>
- Valerio Pascucci and Kree Cole-McLaughlin. 2002. Efficient computation of the topology of level sets. In *IEEE Visualization, 2002. VIS 2002*. IEEE, 187–194.
- Ken Perlin. 2003. Noise, Hypertexture, Antialiasing and Gesture. In *Texturing & Modeling: A Procedural Approach*, David S. Ebert, Kurt Musgrave, Darwyn Peachey, Ken Perlin, and Ken Worley (Eds.). Morgan Kaufmann, 337–412.
- Ronald N Perry and Sarah F Frisken. 2001. Kizamu: A system for sculpting digital characters. In *Proceedings of the 28th annual conference on Computer graphics and interactive techniques*. 47–56.
- Federico Ponchio and Kai Hormann. 2008. Interactive rendering of dynamic geometry. *IEEE transactions on visualization and computer graphics* 14, 4 (2008), 914–925.
- Claude Puech and Hussein Yahia. 1985. Quadrees, octrees, hyperoctrees: a unified analytical approach to tree data structures used in graphics, geometric modeling and image processing. In *Proceedings of the first annual symposium on Computational geometry*. 272–280.
- Inigo Quilez. 2022. *Painting a Landscape with Maths*. Youtube. <https://www.youtube.com/watch?v=BFl4EBO2RE>
- Alexander Raistrick, Lahav Lipson, Zeyu Ma, Lingjie Mei, Mingzhe Wang, Yiming Zuo, Karhan Kayan, Hongyu Wen, Beining Han, Yihan Wang, et al. 2023. Infinite Photorealistic Worlds using Procedural Generation. In *Proceedings of the IEEE/CVF Conference on Computer Vision and Pattern Recognition*. 12630–12641.
- Pedro V Sander and Jason L Mitchell. 2006. Progressive buffers: view-dependent geometry and texture lod rendering. In *ACM SIGGRAPH 2006 Courses*. 1–18.
- Johannes Schmid, Robert W Sumner, Huw Bowles, and Markus H Gross. 2010. Programmable motion effects. *ACM Trans. Graph.* 29, 4 (2010), 57–1.
- Manuel Scholz, Jan Bender, and Carsten Dachsbacher. 2015. Real-time isosurface extraction with view-dependent level of detail and applications. In *Computer Graphics Forum*, Vol. 34. Wiley Online Library, 103–115.
- Dario Seyb, Alec Jacobson, Derek Nowrouzezahrai, and Wojciech Jarosz. 2019. Non-linear sphere tracing for rendering deformed signed distance fields. *ACM Transactions on Graphics* 38, 6 (2019).
- Ruben M Smelik, Tim Tutenel, Rafael Bidarra, and Bedrich Benes. 2014. A survey on procedural modelling for virtual worlds. In *Computer graphics forum*, Vol. 33. Wiley Online Library, 31–50.
- Herman Hansson Söderlund, Alex Evans, and Tomas Akenine-Möller. 2022. Ray Tracing of Signed Distance Function Grids. *Journal of Computer Graphics Techniques Vol 11*, 3 (2022).
- David C. Taylor and William A. Barrett. 1994. An Algorithm for Continuous Resolution Polygonalizations of a Discrete Surface. In *Proc. Graphics Interface '94*. 33–42.
- Ingo Wald, Gregory P Johnson, Jefferson Amstutz, Carson Brownlee, Aaron Knoll, Jim Jeffers, Johannes Günther, and Paul Navrátil. 2016. OSPRay—a CPU ray tracing framework for scientific visualization. *IEEE transactions on visualization and computer graphics* 23, 1 (2016), 931–940.
- Zhou Wang, Alan C Bovik, Hamid R Sheikh, and Eero P Simoncelli. 2004. Image quality assessment: from error visibility to structural similarity. *IEEE transactions on image processing* 13, 4 (2004), 600–612.
- Guthrie H Weber, Oliver Kreylos, Terry J Ligocki, John M Shalf, Hans Hagen, Bernd Hamann, and Kenneth I Joy. 2001. Extraction of crack-free isosurfaces from adaptive mesh refinement data. In *Proceedings of the Joint Eurographics—IEEE TCVG Symposium on Visualization*. Springer, 25–34.
- Rephael Wenger. 2013. *Isosurfaces: geometry, topology, and algorithms*. CRC Press.
- Magnus Wrenning and Jonas Unger. 2018. Synscapes: A photorealistic synthetic dataset for street scene parsing. *arXiv preprint arXiv:1810.08705* (2018).
- Yong Zhou, Baoquan Chen, and Arie Kaufman. 1997. Multiresolution tetrahedral framework for visualizing regular volume data. In *Proceedings. Visualization '97 (Cat. No. 97CB36155)*. IEEE, 135–142.